

Scalable Bayesian divergence time estimation with ratio transformations

Xiang Ji¹, Alexander A. Fisher², Shuo Su³, Jeffrey L. Thorne^{4,5,6}, Barney Potter⁷, Philippe Lemey⁷, Guy Baele⁷, Marc A. Suchard^{*,8,9,10}

¹Department of Mathematics, School of Science & Engineering, Tulane University,
New Orleans, LA, USA

²Department of Statistical Science, Duke University, Durham, NC, USA

³MOE International Joint Collaborative Research Laboratory for Animal Health & Food Safety,
Jiangsu Engineering Laboratory of Animal Immunology, Institute of Immunology, College of
Veterinary Medicine, Nanjing Agricultural University, Nanjing, Jiangsu, China

⁴Bioinformatics Research Center, ⁵Department of Statistics, ⁶Department of Biological Sciences,
North Carolina State University, Raleigh, NC, USA

⁷Department of Microbiology, Immunology and Transplantation, Rega Institute, KU Leuven,
Leuven, Belgium

⁸Department of Biomathematics, ⁹Department of Human Genetics, David Geffen School of
Medicine, ¹⁰Department of Biostatistics, Fielding School of Public Health, University of
California Los Angeles, Los Angeles, CA, USA

*Correspondence: msuchard@ucla.edu

Abstract

Divergence time estimation is crucial to provide temporal signals for dating biologically important events, from species divergence to viral transmissions in space and time. With the advent of high-throughput sequencing, recent Bayesian phylogenetic studies have analyzed hundreds to thousands of sequences. Such large-scale analyses challenge divergence time reconstruction by requiring inference on highly-correlated internal node heights that often become computationally infeasible. To overcome this limitation, we explore a ratio transformation that maps the original $N - 1$ internal node heights into a space of one height parameter and $N - 2$ ratio parameters. To make analyses scalable, we develop a collection of linear-time algorithms to compute the gradient and Jacobian-associated terms of the log-likelihood with respect to these ratios. We then apply Hamiltonian Monte Carlo sampling with the ratio transform in a Bayesian framework to learn the divergence times in four pathogenic virus phylogenies: West Nile virus, rabies virus, Lassa virus and Ebola virus. Our method both resolves a mixing issue in the West Nile virus example and improves inference efficiency by at least 5-fold for the Lassa and rabies virus examples. Our method also makes it now computationally feasible to incorporate mixed-effects molecular clock models for the Ebola virus example, confirms the findings from the original study and reveals clearer multimodal distributions of the divergence times of some clades of interest.

Keywords: Divergence time estimation, Bayesian inference, Hamiltonian Monte Carlo, phylogenetics, pathogens

1 Introduction

Since [Zuckermandl and Pauling \(1962\)](#) proposed the first molecular clock model, the development of more reliable divergence time estimation techniques has thrived. Because evolutionary rate and time are confounded in stochastic models for molecular sequence data, divergence time inference can be improved either via advances in treatment of rates or treatment of times. However, the majority of the effort has centered upon improving the model aspects that describe how evolutionary rates change across the tree while the other confounding component — the evolutionary times — has received less attention.

This imbalance is partly due to the constraints on the node heights imposed by the tree structure. Assuming a rooted tree with the root node on the top and tip nodes at the bottom, an internal node must be higher than its descendant nodes but lower than its parent node. These constraints pose great challenge for inferring internal node heights jointly, such that one typically samples or optimizes the height of one node at a time.

Despite this inference difficulty, divergence time estimation is crucial to provide temporal signals for dating biologically important events, from species divergence to viral transmissions in space and time ([Erwin et al., 2011](#); [Meredith et al., 2011](#); [Düx et al., 2020](#); [Lemey et al., 2020](#)). Repeated breakthroughs in sequencing technologies have led to molecular data accumulating at an ever-increasing pace. The result is often data sets that contain so many sequences that desired divergence time analyses become computationally infeasible. When faced with such obstacles, investigators resort to analyzing only a small proportion of the available data and/or sacrificing statistical rigor and biological plausibility by adopting procedures and models that are flawed but computationally convenient. There is therefore substantial value in reducing the amount of computation necessary for statistically sound divergence time inference.

In [Kishino et al. \(2001\)](#), the authors transform the internal node heights of a phylogeny with contemporaneous data sampled at the same time into a collection of ratios that sum to 1. With a Dirichlet prior distribution, [Kishino et al.](#) were then able to jointly sample all

proportions at one time. Inspired by their pioneering work, we explore a more general ratio transformation, similar to that used in [Fourment and Darling \(2019\)](#), for the internal node heights that one can apply to both serially sampled or contemporaneous data. The ratio transformation serves as a reparameterization that works with any existing phylogenetic models without need for any specific prior. In fact, the proposed ratio transformation keeps the topology-imposed constraints by its construction with the ratios being independent such that they are easy to sample from or optimize on.

We show that one can calculate the transformation and the determinant of the Jacobian matrix of the transformation in linear-time with respect to (w.r.t) the number of tips (N). With the determinant of the Jacobian matrix, one can set up the phylogenetic model w.r.t. the untransformed node heights, but sample from the transformed ratio space. To make use of an advanced linear-time gradient of the log-likelihood algorithm ([Ji et al., 2020](#)), we show that one can transform the gradient w.r.t. the untransformed node heights to the gradient w.r.t. the transformed ratio space with $\mathcal{O}(N)$ calculations. The linear-time gradient transformation enables the application of gradient-based Monte Carlo samplers such as the Hamiltonian Monte Carlo (HMC) method ([Neal, 2011](#)) in the Bayesian framework. HMC shows great potential for improving computational efficiency in many phylogenetic applications ([Dinh et al., 2017](#); [Ji et al., 2020](#); [Baele et al., 2020](#)).

We apply the ratio transformation to simultaneously learn the branch-specific evolutionary rates and the internal node heights of four viral examples. Our method significantly improves inference efficiency with a 5- to 8-fold computational performance increase for our Lassa and rabies virus examples. More interestingly, our West Nile virus example shows that our sampler better approximates the posterior density than do classic univariate samplers that suffer from Markov chain Monte Carlo (MCMC) mixing issues. For an Ebola virus example, we show that our method makes it computationally feasible to employ a relaxed clock model to account for both clade- and branch-specific effects that reveal clearer multi-modal distribution of times for clades of interest.

2 New Approach

In this section, we define necessary notation for deriving the ratio transformation. We then illustrate the transformation from the node heights into the ratio space and its reverse transform. We show that the Jacobian matrix of the transform is a triangular matrix such that its determinant calculation only involves the diagonal elements. We derive linear-time algorithms that transform the gradient of the sequence data log-likelihood w.r.t. the node heights into the gradient w.r.t. the ratio space with complete post- and pre-order traversals. We finish the section with another linear-time algorithm that calculates the gradient of the log-Jacobian term w.r.t. the ratio space.

2.1 Notation

Consider a rooted phylogeny \mathcal{F} with N tips and $N - 1$ internal nodes. Assume that the root node is on the top and the tip nodes are at the bottom of \mathcal{F} . We denote the tip nodes with numbers $1, 2, \dots, N$ and the internal nodes with numbers $N + 1, N + 2, \dots, 2N - 1$ where the root node is $2N - 1$. We denote $\text{pa}(i)$ as the parent node of node i . Any branch on the tree is denoted by the number of the child node that ends it (i.e. branch i connects node $\text{pa}(i)$ to i). We denote t_i as the height (i.e., time) of node i . When i is a tip node (i.e., $i \in \{1, 2, \dots, N\}$), its height is the sampling time. In divergence time estimation, one is interested in estimating the heights of internal nodes.

Without loss of generality, we derive the ratio transform where the tip nodes can be associated with serially sampled data and where the transformation with contemporaneous data is then a special case where all tip node times are identical. We first define epochs such that any internal node belongs to one and only one epoch. We then define a ratio parameter ascribed to each of the internal nodes except for the root.

2.2 Epoch construction and the ratio transformation

For an internal node, we refer to its earliest (i.e. highest) descendant tip node as its *anchor node*. Therefore, the anchor node of an internal node is its closest descendant tip node. To make the anchor nodes consistent and unique, we assign an arbitrary ordering among tip nodes to distinguish those with the same sampling times. For example, we pick the tip node with the smallest node number as the anchor node from all closest tip nodes sampled at the same time. We group all internal nodes with the same anchor node into an epoch. We refer to an epoch by the number of its anchor node. Except for the epoch to which the root node belongs, an epoch is constructed to have a chain structure from its anchor node up to the highest node in the epoch (see Figure 1). We refer to the parent node of the highest node in an epoch as its *connecting node* such that the connecting node of an epoch belongs to another epoch. We treat the root node as the connecting node for epochs of its immediate descendant nodes.

Let t_i denote the node height of node i and $\mathcal{E}(i)$ be the epoch to which node i belongs. We refer to the epoch to which the root node belongs as the starting epoch and assign it as $\mathcal{E}(2N - 1)$. We abuse notation by referring to the j^{th} node of epoch k as k_j . For epoch k that contains m_k internal nodes with strictly positive branch lengths, we have $\{t_{k_1}, t_{k_2}, \dots, t_{k_{m_k}} : t_{k_1} > t_{k_2} > \dots > t_{k_{m_k}} > t_k\}$. We refer to the connecting node of an epoch as the 0^{th} node of an epoch, i.e. $k_0 = \text{pa}(k_1)$. We define $L_k = t_{k_0} - t_k$ as the length of epoch k . For the i^{th} internal node k_i from epoch k (i.e. $i > 0$), we define its ratio parameter r_{k_i} as

$$r_{k_i} = \frac{t_{k_i} - t_k}{t_{k_{i-1}} - t_k}, \quad (1)$$

where t_k is the height of the anchor node of epoch k and $k_{i-1} = \text{pa}(k_i)$. Therefore, one can write the time of an internal node as a function of the ratios and the epoch lengths as

$$t_{k_i} = L_k \prod_{n=1}^i r_{k_n} + t_k. \quad (2)$$

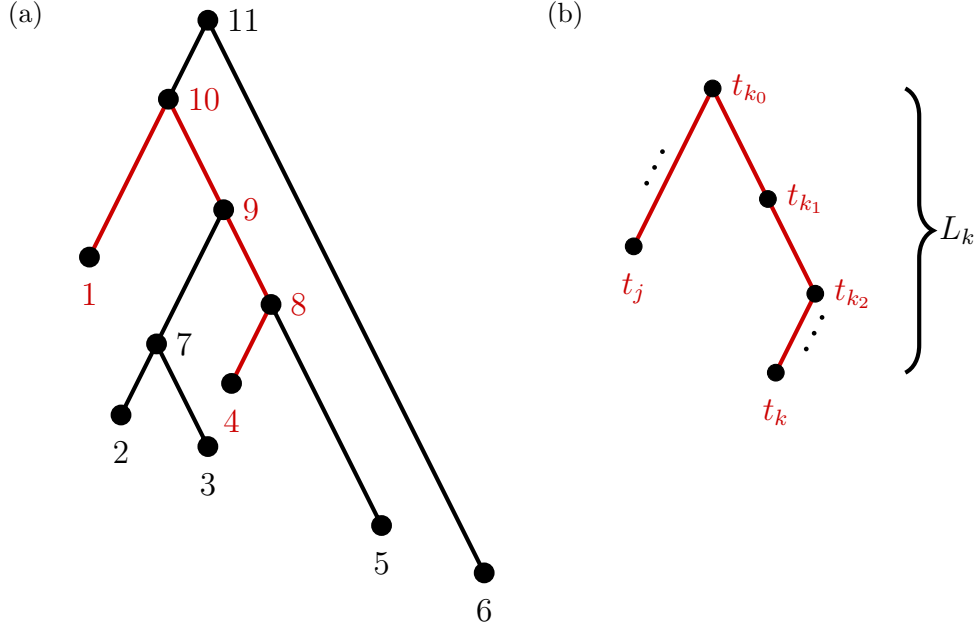


Figure 1: Epoch construction on a 6-taxa tree. (a) Example tree with serially sampled data. (b) One epoch example. For the example tree in (a) with anchor tip 4, $k = 4$, $j = 1$ and $k_0 = 10$. For anchor tip 2, $k = 2$, $j = 4$ and $k_0 = 9$. For anchor tip 1, $k = 1$ is the starting epoch that contains the root node.

To ease notation, let $S_{k_i} = \prod_{n=1}^i r_{k_n}$ be the product of ratios for internal node k_i of epoch k . Equation 2 simplifies to

$$t_{k_i} = L_k S_{k_i} + t_k. \quad (3)$$

Interestingly, there is only one degree of freedom for all epoch lengths because

$$\begin{aligned} t_{k_0} &= t_k + L_k \\ &= t_{\mathcal{E}(k_0)} + L_{\mathcal{E}(k_0)} S_{k_0}, \end{aligned} \quad (4)$$

such that the length of epoch k is determined by the length of the epoch of its connecting node and the two associated anchor node times. We arrive at the following recursive relationship for epoch lengths

$$L_k = t_{\mathcal{E}(k_0)} - t_k + L_{\mathcal{E}(k_0)} S_{k_0}. \quad (5)$$

Therefore, there is effectively only one degree of freedom for the scale of time with all ratios denoting the relative height an internal node has using its parent node and the anchor node as reference. There are many choices for modeling this single dimension for time scale, e.g., one may arbitrarily choose one of the epoch lengths. We pick the starting epoch length as the free parameter $L_{\varepsilon(2N-1)} = t_{2N-1} - t_{\varepsilon(2N-1)}$ which we refer to as the *height parameter* because it represents the height difference from the root node to its closest tip node (all tip nodes are descendants of the root). We refer to the space of the height and $N - 2$ ratio parameters as the *ratio space*. We refer to the space of all untransformed node heights as the *height space*. We refer to the transformation from the height space into the ratio space as the *ratio transform*.

Algorithm 1 illustrates the ratio transform through a single post-order traversal that visits every node on the tree in a descendant-first manner. Likewise, one can perform the inverse ratio transform to get node heights from the ratios by reversing Equation 1 through a pre-order traversal.

Algorithm 1 Ratio transform through a single post-order traversal

```

for node  $i$  in a post-order traversal do
  if  $i$  is a tip node then
    Set the anchor tip of epoch  $i$  as node  $i$ .
  else
    Set the anchor tip of  $i$  the same as the anchor tip of its highest daughter node.
    Calculate  $r_i$  according to Equation 1.
  end if
end for

```

2.3 Gradient and Jacobian

Many modern inference machineries benefit from gradient information to find descending directions of the likelihood surface or to efficiently integrate dynamics along the surface for generating Monte Carlo proposals (e.g. Ji et al. (2020) contains gradient applications in non-linear optimization and Bayesian posterior sampling). When transforming probabil-

ity densities from their original space into another (e.g. the ratio space in this case), one needs the determinant of the Jacobian matrix to correctly “weight” the transformed density (see Theorem 2.1.5 from [Casella and Berger \(2001\)](#)). In this section, we derive algorithms for transforming the “unweighted” likelihood into the ratio space together with the associated quantities from the log-determinant of the Jacobian matrix to correctly set the “weight”.

In [Ji et al. \(2020\)](#), we introduced a linear-time algorithm for calculating the gradient of the log-likelihood w.r.t. the branch length $b_i = \zeta_i(t_i - t_{\text{pa}(i)})$ that is the product of the evolutionary rate ζ_i and the time duration $t_i - t_{\text{pa}(i)}$ of branch i . To calculate the gradient w.r.t. node heights, one starts with the gradient w.r.t. branch lengths and finishes via the chain rule. More specifically, for node i with its two immediate descendant nodes j and k , the derivative of the log-likelihood, $\log \mathbb{P}(\mathbf{Y})$, w.r.t. t_i is:

$$\frac{\partial}{\partial t_i} \log \mathbb{P}(\mathbf{Y}) = \begin{cases} \frac{\partial \log \mathbb{P}(\mathbf{Y})}{\partial b_i} \frac{\partial b_i}{\partial t_i} + \frac{\partial \log \mathbb{P}(\mathbf{Y})}{\partial b_j} \frac{\partial b_j}{\partial t_i} + \frac{\partial \log \mathbb{P}(\mathbf{Y})}{\partial b_k} \frac{\partial b_k}{\partial t_i}, & i \neq 2N - 1 \\ \frac{\partial \log \mathbb{P}(\mathbf{Y})}{\partial b_j} \frac{\partial b_j}{\partial t_i} + \frac{\partial \log \mathbb{P}(\mathbf{Y})}{\partial b_k} \frac{\partial b_k}{\partial t_i}, & i = 2N - 1. \end{cases} \quad (6)$$

It is important to recall that a ratio parameter is only explicit to the node it assigns to and all its descendant nodes by Equation 2. Therefore, we only need the partial derivatives $\frac{\partial t_k}{\partial r_i}$ from node i and all its descendant nodes to finish the chain rule

$$\frac{\partial}{\partial r_i} \log \mathbb{P}(\mathbf{Y}) = \sum_k \left[\frac{\partial}{\partial t_k} \log \mathbb{P}(\mathbf{Y}) \frac{\partial t_k}{\partial r_i} \right]. \quad (7)$$

To derive the partial derivative $\frac{\partial t_k}{\partial r_i}$ for any two nodes i and k such that node k is a descendant of node i , we separate the node pairs into two cases. The first case considers node i and node k in the same epoch (including the pair where $i = k$, e.g. Equation 3), such that

$$\begin{aligned} \frac{\partial t_k}{\partial r_i} &= L_{\mathcal{E}(k)} \frac{\partial S_k}{\partial r_i} \\ &= \frac{t_k - t_{\mathcal{E}(k)}}{r_i}. \end{aligned} \quad (8)$$

For the other case where node i and node k belong to different epochs, we start with revealing the relationship between the partial derivatives of node k 's height t_k and its connecting node $\mathcal{E}(k)_0$'s height $t_{\mathcal{E}(k)_0}$ w.r.t. the same ratio r_i (e.g. plug Equation 5 in Equation 3), such that

$$\begin{aligned} \frac{\partial t_k}{\partial r_i} &= S_k \frac{\partial (t_{\mathcal{E}(k)_0} - t_{\mathcal{E}(k)} + L_{\mathcal{E}(i)} S_{\mathcal{E}(k)_0})}{\partial r_i} \\ &= S_k \frac{\partial t_{\mathcal{E}(k)_0}}{\partial r_i}. \end{aligned} \tag{9}$$

Equation 9 shows that one obtains the partial derivative of a node height t_k w.r.t. ratio r_i by multiplying the related ratio product (i.e. S_k) and the partial derivative of the node height $t_{\mathcal{E}(k)_0}$ w.r.t. ratio r_i (i.e. $\frac{\partial t_{\mathcal{E}(k)_0}}{\partial r_i}$). Combining Equations 8 and 9, we inductively derive a general expression for the derivatives where node i and node k do not belong to the same epoch. We arrive at this derivation through the existence of a series of connecting nodes (when traveling from node k to node i) starting from epoch $\mathcal{E}(k)$ that the last connecting node belongs to the same epoch as node i , i.e. $\mathcal{E}(\mathcal{E}(\dots \mathcal{E}(k)_0)_0) = \mathcal{E}(i)$. The general expression for the derivative becomes

$$\frac{\partial t_k}{\partial r_i} = S_k S_{\mathcal{E}(k)_0} \dots S_{\mathcal{E}(\dots \mathcal{E}(k)_0)_0} \frac{\partial t_{\mathcal{E}(\dots \mathcal{E}(k)_0)_0}}{\partial r_i}. \tag{10}$$

By naively plugging Equation 8 and Equation 10 into Equation 7, we obtain the gradient w.r.t. the ratio space. However, this operation amounts to $\mathcal{O}(N^2)$ computations for transforming the gradient. To overcome this computational burden, we develop a linear-time $\mathcal{O}(N)$ algorithm for transforming the gradient.

2.3.1 Post-order traversal

Consider three internal nodes i , j and k such that node k is the parent node of node i and node j . The linear-time algorithm for transforming the gradient w.r.t. ratio parameters builds on two properties of the ratio transformation. The first property is that any descendant node of node k except node i or node j is a descendant node of either node i or node j (for bifurcating trees). The other property is that node k belongs to the same epoch as either

node i or node j . As is common in dynamic programming algorithms, we want to derive the relationship of $\frac{\partial t_l}{\partial r_k}$ with $\frac{\partial t_l}{\partial r_i}$ and $\frac{\partial t_l}{\partial r_j}$ where node l is descendant of node k to reuse quantities cached from evaluating Equation 7 on descendant nodes. More specifically, we want to reuse the summations already determined for $\frac{\partial}{\partial r_i} \log \mathbb{P}(\mathbf{Y})$ and $\frac{\partial}{\partial r_j} \log \mathbb{P}(\mathbf{Y})$ when calculating $\frac{\partial}{\partial r_k} \log \mathbb{P}(\mathbf{Y})$ as in Equation 9.

Without loss of generality, we assume node k belongs to the same epoch as node i . The following relationships between derivatives w.r.t. the three ratio parameters r_i , r_j and r_k enable the linear-time algorithm through a single post-order traversal to update the gradient from the node height space into the ratio space. From Equation 8 and Equation 10, when node l is a descendant of node i (including $i = l$) such that node k and node l are in the same epoch,

$$\frac{\partial t_l}{\partial r_k} = \frac{\partial t_l}{\partial r_i} \frac{r_i}{r_k}. \quad (11)$$

When node l is descendant of node j (including $j = l$) such that node k is the connecting node to the epoch $\mathcal{E}(j)$ where node j is the first node,

$$\frac{\partial t_l}{\partial r_k} = \frac{\partial t_l}{\partial r_j} \frac{r_j}{L_{\mathcal{E}(j)}} \frac{\partial t_k}{\partial r_k}. \quad (12)$$

Note that we model the ratio parameters as independent of each other, i.e. $\frac{\partial r_k}{\partial r_i} = \frac{\partial r_k}{\partial r_j} = 0$. Equation 11 and Equation 12 come from the special structure of the transform that the node height of an internal node is a product of a series of ratio parameters with one single height parameter. Algorithm 2 illustrates updating the gradient w.r.t. all ratio parameters (except for the height parameter) where one reuses the derivatives of the log-likelihood w.r.t. two immediate descendant nodes (i.e. nodes i and j) to calculate the derivative of the log-likelihood w.r.t. the parent node (i.e. node k).

Algorithm 2 Transforming the gradient of the log-likelihood w.r.t. ratio parameters by post-order traversal

for node k in a post-order traversal **do**
 if k is a tip node **then**
 Set the gradient of k as 0.
 else
 Let node i and node j be the two immediate descendant nodes of node k
 such that node i and node k belong to the same epoch.
 Set the gradient of k as

$$\frac{\partial}{\partial r_k} \log \mathbb{P}(\mathbf{Y}) = \frac{\partial}{\partial r_i} \log \mathbb{P}(\mathbf{Y}) \frac{r_i}{r_k} + \frac{\partial}{\partial r_j} \log \mathbb{P}(\mathbf{Y}) \frac{r_j}{L_{\mathcal{E}(j)}} \frac{\partial t_k}{\partial r_k} + \frac{\partial}{\partial t_k} \log \mathbb{P}(\mathbf{Y}) \frac{\partial t_k}{\partial r_k}.$$

 end if
end for

2.3.2 Pre-order traversal

We now update the gradient of the log-likelihood w.r.t. the height parameter which is the only dimension left in the ratio transform. We use a pre-order traversal to update the gradient in this dimension because the transformation of all internal node heights depends on it. The update is

$$\frac{\partial}{\partial L_{\mathcal{E}(2N-1)}} \log \mathbb{P}(\mathbf{Y}) = \sum_k \left[\frac{\partial}{\partial t_k} \log \mathbb{P}(\mathbf{Y}) \frac{\partial t_k}{\partial L_{\mathcal{E}(2N-1)}} \right]. \quad (13)$$

Based on Equation 4, we calculate all the partial derivatives $\frac{\partial t_k}{\partial L_{\mathcal{E}(2N-1)}}$ according to Algorithm 3 through a single pre-order traversal.

Algorithm 3 Transforming gradient of the log-likelihood w.r.t. the height parameter by pre-order traversal

for node k in a pre-order traversal **do**
 if k is the root node **then**
 Set the derivative of node height k w.r.t. height parameter as 1 (i.e. $\frac{\partial t_{2N-1}}{\partial L_{\mathcal{E}(2N-1)}} = 1$).
 else
 Set the derivative of k as the product of r_k and the derivative of its parent node
 w.r.t. height parameter (i.e. $\frac{\partial t_k}{\partial L_{\mathcal{E}(2N-1)}} = r_k \frac{\partial t_{\text{pa}(k)}}{\partial L_{\mathcal{E}(2N-1)}}$).
 end if
end for

2.3.3 Determinant of the Jacobian matrix

We now derive the Jacobian matrix associated with the ratio transform whose determinant sets the weight for the transformed density. One derives the full Jacobian matrix for the ratio transform by applying Equation 8 and Equation 10. Note the special structure that has $\frac{\partial t_k}{\partial r_i} \neq 0$ if and only if $i = k$ or node k is descendant of node i , and also note the independence between the height parameter and the ratio parameters. By ordering the entries in a descendant node first fashion that coincides with how nodes are visited in a post-order traversal, the Jacobian matrix becomes triangular (including the height parameter). Because the determinant of a triangular matrix only involves the diagonal entries, the determinant of the Jacobian matrix \mathbf{J} becomes

$$\begin{aligned} |\mathbf{J}| &= \prod_i \frac{\partial t_i}{\partial r_i} \\ &= \prod_i [t_{\text{pa}(i)} - t_{\mathcal{E}(i)}]. \end{aligned} \tag{14}$$

2.3.4 Gradient of log-determinant of the Jacobian matrix

We complete this section with a final linear-time algorithm for calculating the gradient of the log-determinant of the Jacobian matrix w.r.t. the ratio space for applying HMC on this transformed space as described in the next section. This additional gradient component facilitates using HMC to sample all dimensions jointly in the ratio space. Similar to the case of updating the gradient of the log-likelihood from the original space into the ratio space, naively applying Equation 8 and Equation 10 results in an undesired quadratic computational load. One can benefit from the same properties that lead to Algorithm 2 with a modified two-pass linear-time Algorithm 4 that calculates all the derivatives of the log-determinant of the Jacobian matrix w.r.t. the ratio parameters.

Algorithm 4 Calculating gradient of the log-determinant of the Jacobian matrix w.r.t. ratio parameters by post-order traversal

for node k in a post-order traversal **do**

if k is a tip node **then**

$$\frac{\partial}{\partial r_k} \log |\mathbf{J}| = 0$$

else

 Let node i and node j be the two immediate descendant nodes of node k such that node i and node k belong to the same epoch, and compute

$$\frac{\partial}{\partial r_k} \log |\mathbf{J}| = \frac{\partial}{\partial r_i} \log |\mathbf{J}| \frac{r_i}{r_k} + \frac{\partial}{\partial r_j} \log |\mathbf{J}| \frac{r_j}{L_{\varepsilon(j)}} \frac{\partial t_k}{\partial r_k} + \frac{1}{t_k - t_{\varepsilon(k)}} \frac{\partial t_k}{\partial r_k} .$$

end if

end for

for every internal node k **do**

 Update $\frac{\partial}{\partial r_k} \log |\mathbf{J}| = \frac{\partial}{\partial r_k} \log |\mathbf{J}| - \frac{1}{r_k} .$

end for

2.4 Hamiltonian Monte Carlo

HMC is a state-of-the-art MCMC method that generates efficient proposals through Hamiltonian dynamics (Neal, 2011) for the Metropolis-Hastings algorithm (Metropolis et al., 1953). For an arbitrary and unbounded parameter of interest $\boldsymbol{\theta}$ with the posterior density $\pi(\boldsymbol{\theta})$, HMC introduces an auxiliary parameter \mathbf{p} and samples from the product density $\pi(\boldsymbol{\theta}, \mathbf{p}) = \pi(\boldsymbol{\theta})\pi(\mathbf{p})$ through:

$$\begin{aligned} \frac{d\mathbf{p}}{dt} &= -\nabla U(\boldsymbol{\theta}) = \nabla \log \pi(\boldsymbol{\theta}) \text{ and} \\ \frac{d\boldsymbol{\theta}}{dt} &= \nabla K(\mathbf{p}) = \mathbf{M}^{-1}\mathbf{p}, \end{aligned} \tag{15}$$

where $U(\boldsymbol{\theta})$ is the ‘potential energy’ often set to the negative log-posterior density and $K(\mathbf{p}) = \mathbf{p}'\mathbf{M}^{-1}\mathbf{p}/2$ is the ‘kinetic energy’ as the auxiliary parameter \mathbf{p} typically follows a multivariate normal distribution $\mathbf{p} \sim \mathcal{N}(\mathbf{0}, \mathbf{M})$ with a ‘mass matrix’ \mathbf{M} as the covariance matrix. HMC has shown great potential in diverse phylogenetic applications (Dinh et al., 2017; Ji et al., 2020; Baele et al., 2020).

Naive application of HMC on the space of internal node heights is highly inefficient because of the irregular constraints on these parameters. Instead, the ratio space is trivial to extend such that it is unbounded by applying a logit-transform to each ratio independently

and a log-transform to the single height parameter. We apply HMC on the (extended) ratio space for efficient sampling of all internal node heights. Finally, we also apply HMC for jointly sampling the evolutionary rates and times (i.e. divergence time estimation) and explore the additional efficiency gain this affords.

Preconditioning with adaptive variance The geometric structure of the posterior distribution significantly affects the computational efficiency of HMC. For example, when the scales of the posterior distribution vary among individual parameters, failing to account for such structure may reduce the efficiency of HMC (Neal, 2011; Stan Development Team, 2017; Ji et al., 2020). We can adapt HMC for such structure by modifying the dynamics in Equation 15 via an appropriately chosen mass matrix \mathbf{M} . In Ji et al. (2020), we employ a mass matrix informed by the diagonal entries of the Hessian matrix of the log-posterior to account for the variable scales among dimensions. Unfortunately, one needs the full Hessian matrix in the original height space to transform into the Hessian matrix w.r.t. the ratio space. This strategy is too computationally expensive to adopt.

To incorporate information from the covariance matrix without excessive computational burden, we seek an alternative adaptive MCMC procedure (Haario et al., 1999; Andrieu and Thoms, 2008; Roberts and Rosenthal, 2009). Adaptive MCMC has previously found its way into Bayesian phylogenetic inference (Baele et al., 2017) and we use this technique here to tune \mathbf{M} to the covariance matrix estimated from previous samples in the Markov chain. We further restrict \mathbf{M} to remain diagonal and hence to scale the ratio dimensions according to their marginal covariance. This restriction is commonly imposed to regularize the estimate, and a diagonal matrix alone can greatly enhance sampling efficiency of HMC in many situations (Stan Development Team, 2017; Salvatier et al., 2016; Ji et al., 2020). We start the HMC sampler with an identity \mathbf{M} matrix to collect an initial set of samples (e.g. 200 in our analyses), after which we employ the sample covariance to tune \mathbf{M} adaptively. Also, we only update the diagonal mass matrix every 10 HMC iterations so that the cost of

computing the adaptive M diagonals remains negligible.

2.5 Emerging viral sequences

We examine the molecular evolution of West Nile virus (WNV) in North America (1999 - 2007), rabies virus (RABV) in the United States (1982 - 2004), the S segment of Lassa virus (LASV) in West Africa (2008 - 2013) and Ebolavirus (EBOV) in the Democratic Republic of Congo, Africa (2018 - 2020) (Pybus et al., 2012; Biek et al., 2007; Andersen et al., 2015; Mbala-Kingebeni et al., 2021). In all four virus data sets, phylogenetic analyses have revealed a high variation of the evolutionary rates across branches in the underlying phylogeny.

West Nile virus West Nile virus is a mosquito-borne RNA virus that involves multiple species of mosquitoes and birds where birds are the primary host. WNV first emerged in the Americas in New York in 1999, and quickly spread across the continent, causing an epidemic of human disease accompanied with massive bird deaths. In total, human infections have resulted in over 48,000 reported cases, 24,000 reported neuroinvasive cases, and over 2,300 deaths (Hadfield et al., 2019). The molecular sequences consist of 104 full genomes, with a total alignment length of 11,029 nucleotides, and were collected from infected human plasma samples from 2003 to 2007 as well as near-complete genomes obtained from GenBank (Pybus et al., 2012).

Rabies virus Rabies is an RNA virus that can cause zoonotic disease and is responsible for over 50,000 human deaths every year. Besides bats, several terrestrial carnivore species, such as raccoons are important rabies reservoirs. Before the detection of a raccoon-specific rabies virus variant in 1970s, the limited focus of raccoons as a primary host for rabies was in the southeastern U.S., particularly Florida. Over the following decades, an emergence of the virus spread along the mid-Atlantic coast and northeastern U.S. We analyze the molecular sequences originally described in Biek et al. (2007) that previously served as an example dataset in work on the flexible non-parametric skygrid coalescent model (Gill et al., 2016).

The data consist of 47 sequences sampled from rabid raccoons between 1982 and 2004 that contain the complete rabies nucleoprotein gene (1365 bp) with part of a noncoding region (87 bp) immediately following its 3' end, and a large portion of the glycoprotein gene (1359 bp).

Lassa virus Lassa virus is the causative agent of Lassa fever, a hemorrhagic fever endemic to parts of West Africa that is responsible for thousands of deaths and tens-of-thousands of hospitalizations each year ([Andersen et al., 2015](#)). LASV infections can lead to Lassa fever, a hemorrhagic fever similar to that from EBOV and endemic to parts of West Africa. Despite the fact that Lassa fever can lead to over 50% fatality rates among hospitalized patients, an effective vaccine for LASV has yet to be developed and approved. Unlike EBOV (see next paragraph), which passes directly between humans, LASV circulates in a rodent (*Mastomys natalensis*) reservoir and mainly infects humans through contact with rodent excreta. The LASV genome is comprised of two negative-sense single-stranded RNA segments: the L segment is 7.3 kilobase pairs (kb) long, and the S segment is 3.4 kb long. In this paper, we use the S segment of the LASV sequence data set of [Andersen et al. \(2015\)](#) that consists of 211 samples obtained at clinics in both Sierra Leone and Nigeria, rodents in the field, laboratory isolates and previously sequenced genomes.

Ebola virus The Ebola virus disease (EVD) outbreak in North Kivu province in the Democratic Republic of Congo (DRC) during 2018 - 2020 was the world's second largest Ebola outbreak on record. It led to 3,481 total cases with 2,299 deaths ([World Health Organization, 2021](#)). One patient who received the recombinant vesicular stomatitis virus-based vaccine was diagnosed with EVD and recovered within 14 days after treatment. However, 6 months later, the same patient presented again with severe EVD-like illness and EBOV viremia and died ([Mbala-Kingebeni et al., 2021](#)). The molecular sequences consist of 297 sequenced isolates that contain 72 epidemiologically-linked cases to the patient's second infection.

2.6 Mixed-effects relaxed clock model

We employ mixed-effects relaxed clock models to learn the evolutionary rates of the four viral datasets as detailed in [Bletsa et al. \(2019\)](#). More specifically, we use the same random-effects relaxed clock model detailed in [Ji et al. \(2020\)](#) for the analysis of WNV, RABV and LASV datasets. For the EBOV example, we use a mixed-effects relaxed clock model with clade-specific fixed-effects to model clade-specific rate variations among the three branches leading to three clades of interest (relapse clade, MAN14985 clade and KAT21596 clade). The use of the clade-specific fixed-effects mimics a local clock model that allows us to model and compare possibly different evolutionary rates of persistent infection and overall outbreak, but has previously not been computationally feasible.

3 Results

We summarize the computational efficiency improvement with HMC on the ratio space followed by our biological findings on divergence time estimations of the four examples.

3.1 Computational performance

We infer the posterior distribution of all internal node heights using two different MCMC transition kernels implemented in BEAST ([Suchard et al., 2018](#)) with likelihood computations off-loaded to the high-performance BEAGLE library ([Ayres et al., 2019](#)) (see [Section 5](#) for more details). The first transition kernel proposes new values for one internal node height at a time from their support. This represents the current best-practice approach used in BEAST and we will refer to this kernel as “univariable”. The other transition kernel utilizes HMC with a diagonal mass matrix informed by adaptive variance on the ratio space that we will refer to as “HMC”. As is conventional for Bayesian phylogenetics, we employ a Metropolis-within-Gibbs ([Tierney, 1994](#); [Andrieu et al., 2003](#)) inference strategy that cycles between sampling the tree, the evolutionary rates and then other phylogenetic modeling

parameters, each from their respective full conditional distributions.

As expected, sampling the topology and the high-dimensional rate and time (i.e., node height) parameters is computationally rate-limiting. Therefore, we explore two scenarios: (1) we sample divergence times only in scenario “time”; and (2) we sample evolutionary rate and time jointly in scenario “rate & time”. We compare the efficiency of these transition kernels through their effective sample size (ESS) per unit time for divergence time estimations. For each analysis, we run the MCMC iterations with each of the transition kernels for roughly the same run time (see Section 5 for more details of chain lengths from supplementary BEAST XML files). To maintain identifiability of internal nodes, we constrain the comparisons of the WNV, RABV and LASV examples to a fixed topology that was randomly selected from its posterior distribution. The topologies of the WNV and LASV examples are the same as in Ji et al. (2020). We relax the topology constraint (i.e. not fixing the tree topology) for the EBOV example. We present the computational efficiency improvement with HMC in the ratio space for sampling node heights. The application of HMC on the ratio dimensions greatly improves the mixing of the MCMC chain whereas the univariable samplers are problematic for learning the height of some internal nodes that are close to the root in the WNV example.

Figure 2 illustrates the posterior sampling efficiency with HMC and univariable samplers in terms of ESS per unit time. We exclude the WNV example from the efficiency comparison because the poor mixing with univariable samplers leads to an inflated speed-up for HMC. Table 1 shows the summary statistics of the efficiency gain of the HMC sampler compared with the univariable samplers for the three examples. The HMC sampler gains at least 5-fold efficiency improvement in terms of the minimum ESS per unit time in the RABV and LASV examples that have no difficulties of mixing for the univariable sampler.

3.2 Divergence time estimations

We summarize divergence time estimation results for each of the viral examples.

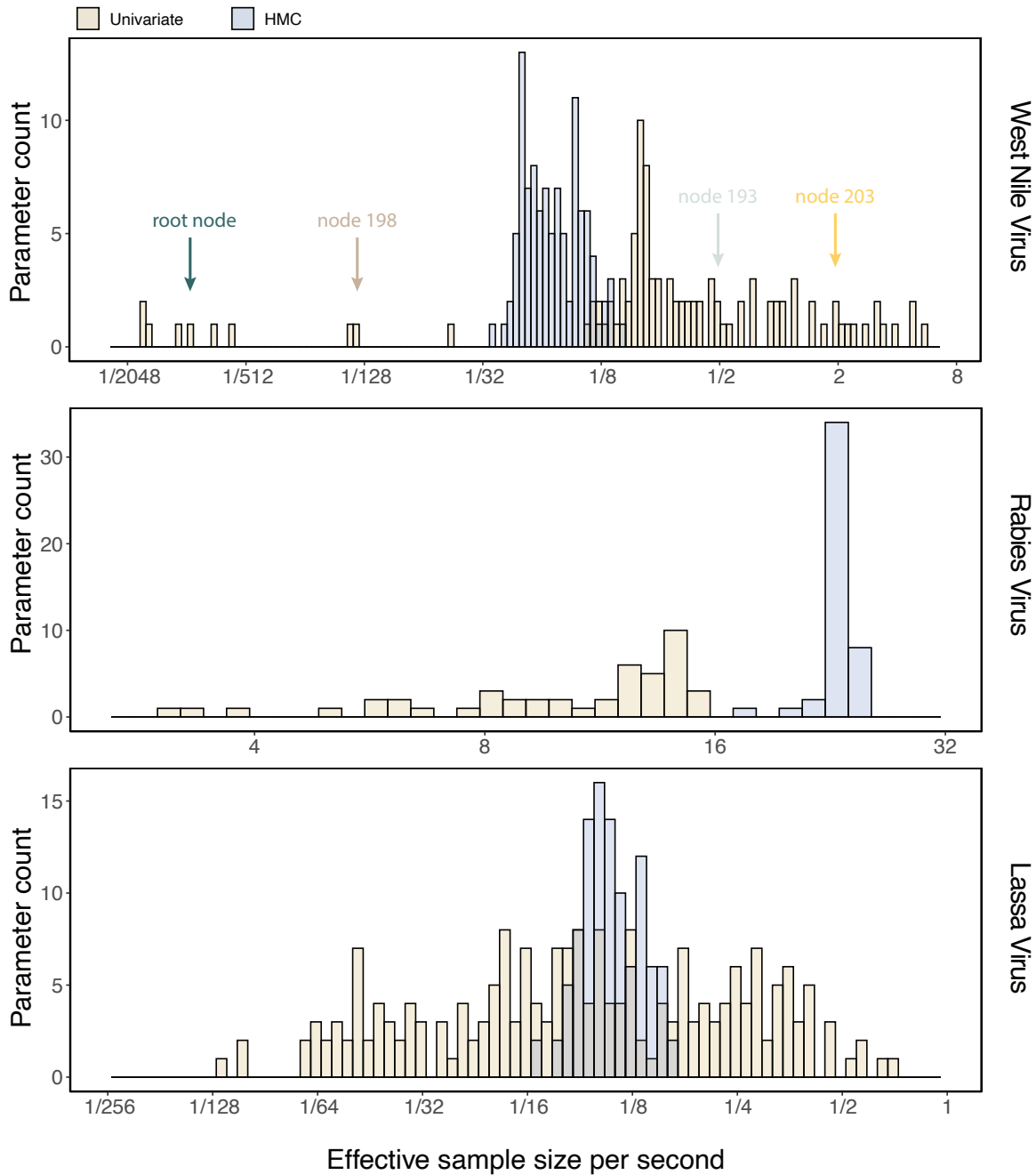


Figure 2: Posterior sampling efficiency on all node height parameters for the WNV, RABV, and LASV examples. We bin parameters by their ESS/s values. The two transition kernels employed in the MCMC are color-coded: a univariable transition kernel and an HMC transition kernel with an adaptive mass matrix.

ESS/s		univariable		HMC		Speedup	
		minimum	median	minimum	median	minimum	median
RABV	time	3.187	12.154	17.358	23.579	5.4×	1.9×
	rate & time	0.927	4.638	6.324	8.355	6.8×	1.8×
LASV	time	0.008	0.090	0.065	0.107	7.9×	1.2×
	rate & time	0.002	0.016	0.018	0.040	8.0×	2.4×

Table 1: Computational performance of transition kernels for the RABV and LASV examples. Computational efficiency measured in terms of effective sample size per second (ESS/s). We compare the performance of our HMC transition kernels operating on the transformed ratio space with a univariable (univariable) transition kernel on the original node height space. We report speedup with respect to the minimum and median ESS/s (listed in the columns of “univariable” and “HMC”) across parameters for each example and method. We do not report the unreliably high speed-ups for the WNV dataset because of mixing issues under the “univariable” kernel.

West Nile virus Our analysis estimates the tree-wise (fixed-effect) rate with posterior mean 5.67 (95% Bayesian credible interval: 5.05, 6.30) $\times 10^{-4}$ substitutions per site per year and an estimated variability characterized by the scale parameter of the lognormal distributed branch-specific random-effects with posterior mean 0.34 (0.21, 0.47). These values are similar to previous estimates (Pybus et al., 2012; Ji et al., 2020). Figure 3 shows the maximum clade credible evolutionary tree of the WNV example as well as trace plots of several nodes of interest. Our analysis estimates the date of the epidemic origin to have posterior mean 1998.6 (1997.8, 1999.1) and this is similar to previous estimates. Matching previous findings that the American epidemic was likely to originate from the introduction of a single highly pathogenic lineage, our analysis infers the NY99 lineage to be basal to all other genomes.

Of important note, the MCMC chain suffers from mixing for some height dimensions close to the root (including the root) under the “univariable” kernel as illustrated by the traceplot in Figure 3 (B) I and II. The mixing issue propagates from the root node to a few of its descendant nodes (e.g. node 198) that plagues over these dimensions because univariable samplers propose a new value for an internal node’s height from the interval set by the height of its parent and closest descendant node. Such a tree-like boundary structure

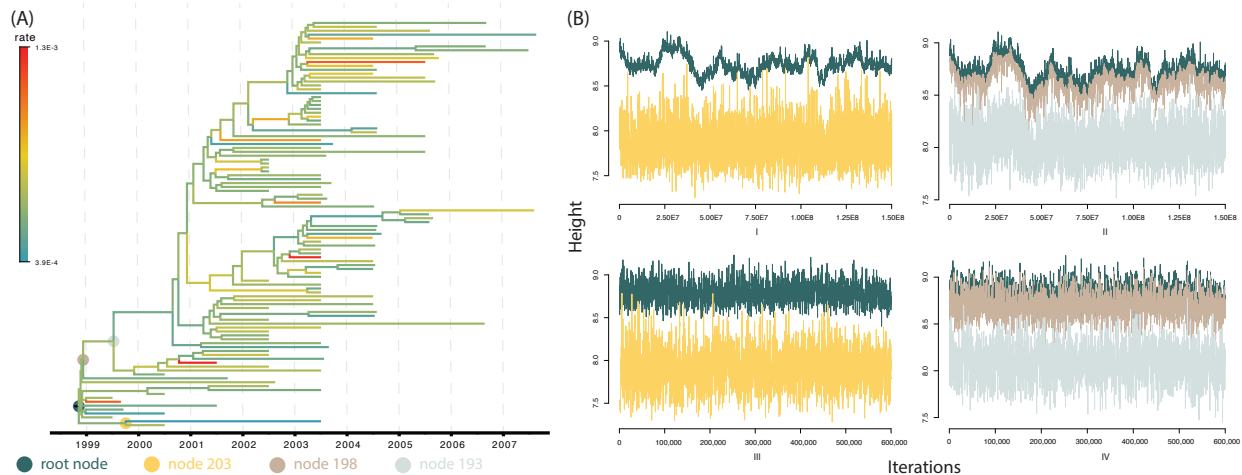


Figure 3: Trace plot of four height parameters indicated on the WNV phylogeny. (A) The WNV phylogeny explored in the example. Branches on the tree are color-coded by the posterior means of the branch-specific evolutionary rates. Four representative nodes indicated by colored dots on the tree illustrate mixing issues at nodes close to the root when learning the posterior distribution of their heights using the univariable samplers. (B) The trace plot of the height parameter of the four nodes indicated in (A) using the same color scheme. I. and II. are trace plots with the univariable samplers for an MCMC chain of length 1.5×10^8 iterations. III. and IV. are trace plots with the HMC sampler for an MCMC chain of length 600,000.

requires multiple height changes on an internal node and the nodes setting its boundaries in the same direction before a “big” move is possible that often fails by one of these dimensions moving at the opposite direction.

Rabies virus Our analysis results in a posterior mean rate of $2.12 (1.73, 2.51) \times 10^{-4}$ substitutions per site per year. The estimated scale parameter has posterior mean 0.10 (0.00, 0.24). Figure 4 shows the maximum clade credible evolutionary tree of the RABV example. Our analysis estimates the date of the root of the tree to be 1971.9 (1951.3, 1979.7). This is slightly older than the estimate in [Biek et al. \(2007\)](#) and our 95% Bayesian credible interval is wider.

Lassa virus Our analysis yields a posterior mean rate of $0.97 (0.81, 1.14) \times 10^{-3}$ substitutions per site per year. The estimated scale parameter has posterior mean 0.089 (0.035, 0.140).

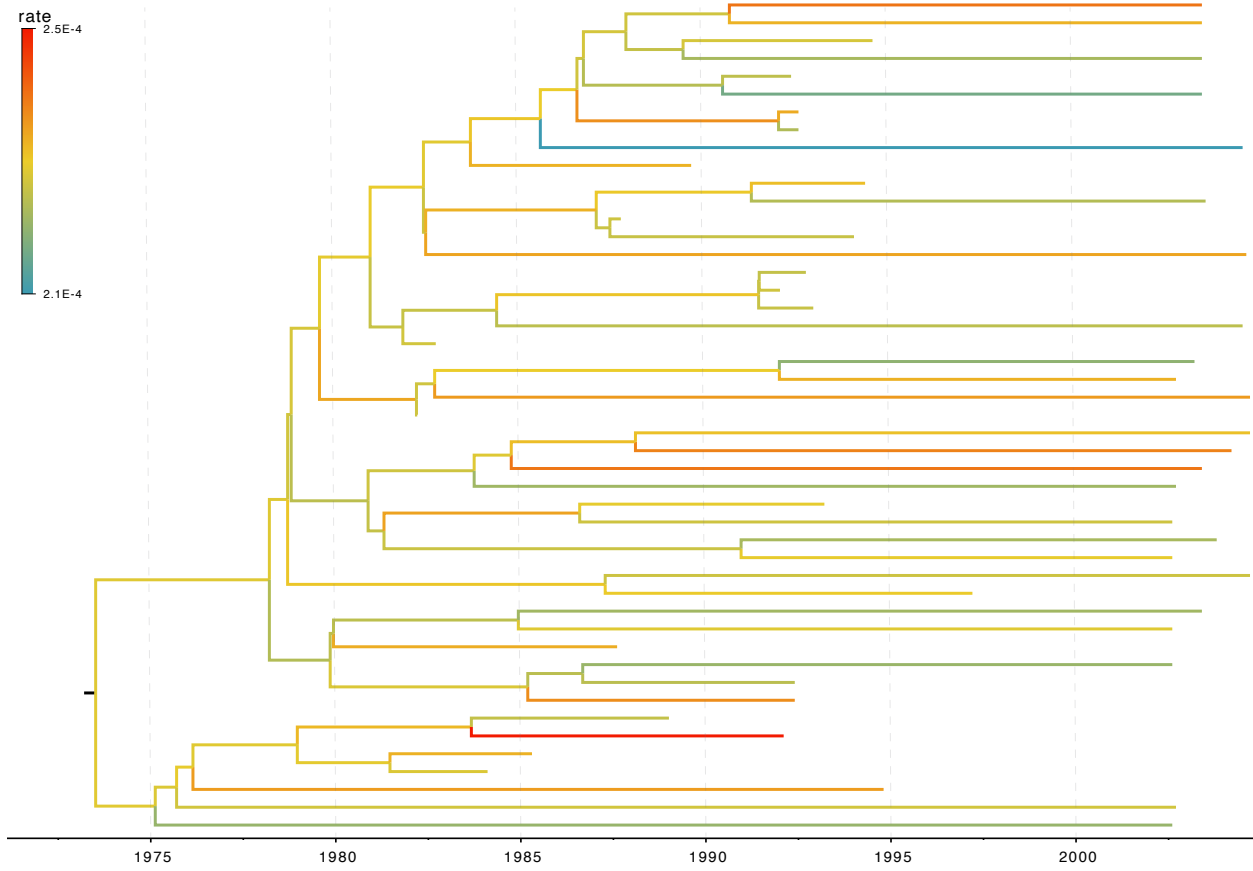


Figure 4: The RABV phylogeny explored in the example. Branches on the tree are color-coded by the posterior means of the branch-specific evolutionary rates.

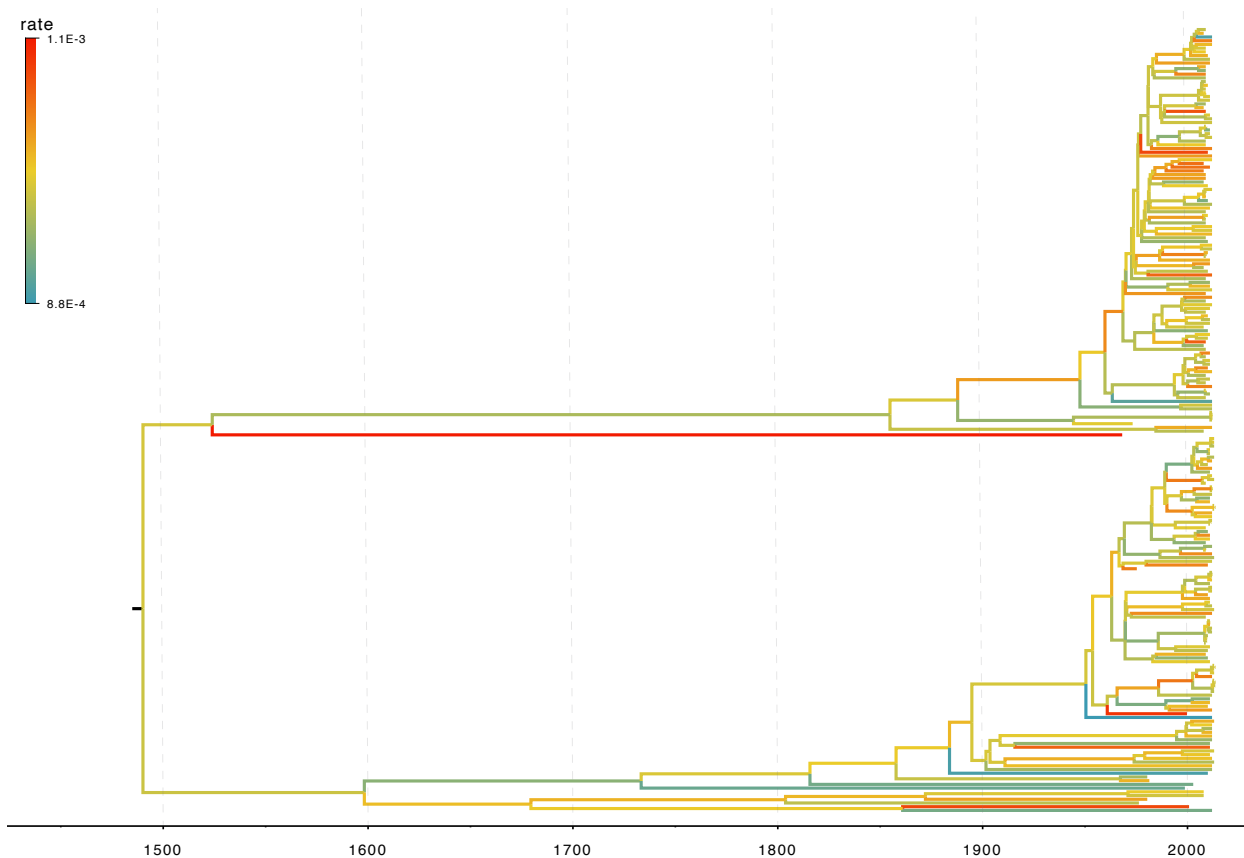


Figure 5: The LASV phylogeny explored in the example. Branches on the tree are color-coded by the posterior means of the branch-specific evolutionary rates.

Figure 5 shows the maximum clade credible evolutionary tree of the LASV example. The date of the root of the tree is inferred to be 1434.0 (1059.0, 1601.7). This agrees with the finding by Andersen et al. (2015) that LASV is a long-standing human pathogen whose most recent common ancestor existed around six hundred years ago.

Ebolavirus Our analysis yields a posterior mean rate $7.70 (6.63, 8.82) \times 10^{-4}$ substitutions per site per year. The scale parameter has posterior mean 0.98 (0.64, 1.33). Figure 6 shows the maximum clade credible evolutionary tree of the EBOV example. The inferred MCC tree shows a significant slow-down in evolutionary rate on the branch leading to the relapse clade that roughly spans over 5.3 months, similar to the discovery from Mbala-Kingebeni et al. (2021). However, our analysis reveals more variability in evolutionary rates compared

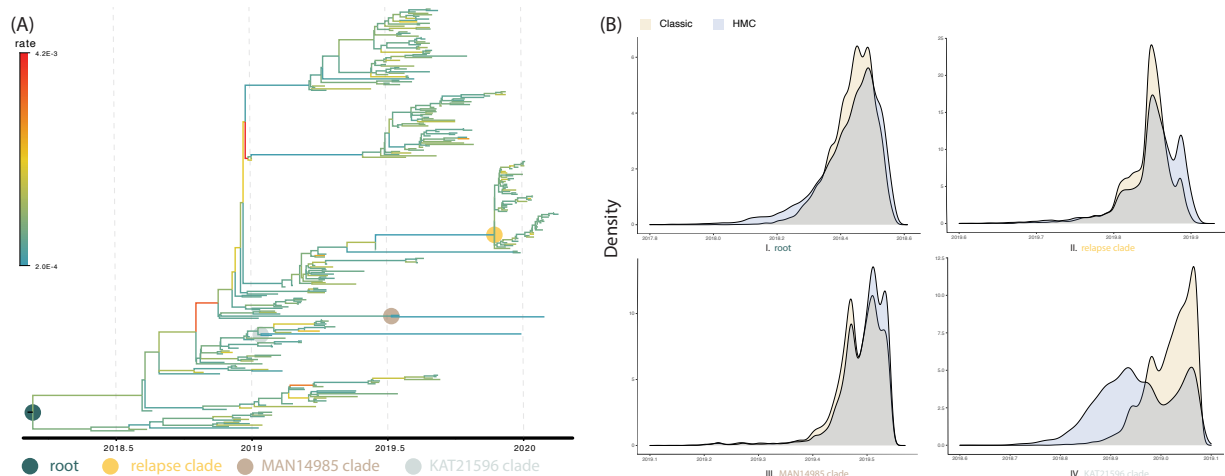


Figure 6: Kernel density estimation plot of the tMRCA distribution of four clades of interest on the EVD phylogeny. (A) The EVD phylogeny explored in the example. Branches on the tree are color-coded by the posterior means of the branch-specific evolutionary rates. We use four colored dots to indicate the four MRCA nodes of four clades of interest on the tree. (B) The kernel density estimation plot of the tMRCA of the four nodes indicated in (A).

to the original study. The MAN4194 sequence that was collected from the individual with the relapsed Ebola infection is basal to all other DRC sequences within the relapse clade. Our analysis estimates the date of most recent common ancestor (MRCA) of the relapse clade (Figure 6 B II) to be 2019.85 (2019.77, 2019.91). This is similar to the estimate of Mbala-Kingebeni et al. (2021). However, our analysis revealed a clearer bimodal posterior distribution that was previously missed. Our estimated date of the MRCA of the MAN14985 clade (Figure 6 B III) is 2019.49 (2019.42, 2019.54) and the estimated date of the MRCA of the KAT21596 set (Figure 6 B IV) is 2018.96 (2018.83, 2019.07).

4 Discussion

The confounding of evolutionary rate and time has imparted divergence time estimation with high uncertainty and low reliability of the inference. Nonetheless, much effort and improvement have shaped the molecular clock models to better characterize evolutionary rate heterogeneity along phylogenies (Thorne et al., 1998; Kishino et al., 2001; Drummond et al.,

2006; Rannala and Yang, 2007; Lemey et al., 2010; Lartillot et al., 2016; Bletsas et al., 2019).

We here introduce a linear-time transformation of the internal node height parameters into a ratio space with the aim to improve estimation efficiency under complex molecular clock models. Naive transformation of the gradient of the log-likelihood from the original height space into the ratio space results in $\mathcal{O}(N^2)$ computations. To make the transformation scalable, we present linear-time algorithms that improve the performance of this transformation. With a slight modification, Algorithm 4 builds upon Algorithm 2 to calculate all derivatives of the log-determinant of the Jacobian matrix also in linear-time. This collection of linear-time algorithms enables researchers to employ dynamic-based samplers (e.g., HMC) to sample the internal node heights and substantially improve inference.

When applying HMC on all dimensions in the ratio space, the sampler proposes a new set of values for the height parameter and all ratios which corresponds to a set of new values for all internal node heights in the original height space. Alternatively, one may cycle HMC on subsets of dimensions from the ratio space in a Metropolis-within-Gibbs inference strategy such that in each iteration, HMC proposes new values to only a subset of dimensions. For example, one possible choice of these subsets is to separately sample the root height and all the ratios (i.e. one subset containing only the height parameter and one subset containing all ratio parameters). Interestingly, each of the two subsets takes a full traversal for updating the gradient through Algorithms 2 and 3 where the postorder traversal updates the gradient w.r.t. all ratio parameters ($N-2$ dimensional) and the preorder traversal updates only the height parameter (single dimensional). Therefore, sometimes it might be more computationally efficient to mix the classic univariable sampling kernels with HMC for the height dimension to benefit from the low computational load for learning the root height dimension. For example, one may apply classic univariable samplers on the height dimension in ratio space instead of HMC. In addition, one may apply classic univariable samplers on the original root height dimension such that with careful caching of the previous iteration, each proposal only needs updating two postorder partial likelihood vectors corresponding to

the two immediate descendant branches from the root. However, as illustrated by the WNV example, classic univariable samplers may suffer from the constraints on the node heights resulting in poor mixing in some dimensions (e.g. several internal nodes close to the root in this case), where the mixture of samplers may lead to worse computational efficiency. To investigate the univariable sampler’s validity, we ran the chain 10x longer for the WNV example. As expected, the trace plot of the longer chain exhibits a normal “caterpillar” shape that indicates both the validity and limitation of the univariable samplers.

The EBOV example employs a more general mixed-effects relaxed clock model with clade-specific fixed-effects and branch-specific random-effects. The original study ([Mbala-Kingebeni et al., 2021](#)) incorporates rate variation into a strict molecular clock model by introducing a single parameter to capture fixed-effects from the clades of interest. Their molecular clock model therefore has 2 dimensions. The mixed-effects model employed in this study now utilizes a 597-dimensional parameter (4 dimensions for clade-specific fixed-effects with an intercept term, 592-dimensions for branch-specific random-effects, and 1 dimension for the scale parameter) to capture multiple sources of rate variation. This more general mixed-effects model detects the same slow-down of the evolutionary rate of the branch leading to the relapse clade. Interestingly, the relapse clade and the MAN14985 clade are monophyletic with posterior probability approaching 1 in our analyses whereas the KAT21596 clade is monophyletic with posterior probability 0.37 compared to the posterior probability of 0.95 in the original study. The lower posterior probability estimate for the two sequences (KAT21596 and BTB4325) forming a monophyletic clade indicates a different mixture of tree topologies partly owing to the more general molecular clock model and potentially better mixing of node heights in each topology. The difference in posterior probability of the KAT21596 clade further affects the multi-modal posterior distribution of tMRCA of the two sequences as in [Figure 6 \(B\)](#).

Recent molecular clock models add additional dependence of evolutionary rate onto time ([Aiewsakun and Katzourakis, 2015](#); [Ho et al., 2015](#); [Membrebe et al., 2019](#)) that bring in

more biological insights into the time-dependency of the evolutionary rates in viral evolution. However, such a dependence structure further complicates the confounding of evolutionary rate and time. Fortunately, the complex dependence structure only affects the derivatives without influencing the ratio transformation or the HMC machinery and is therefore the reason Equation 6 uses more general terms $\frac{\partial b_i}{\partial t_i}$, $\frac{\partial b_j}{\partial t_i}$, and $\frac{\partial b_k}{\partial t_i}$.

A caveat of the linear-time algorithms that are introduced here is that they assume sampling dates are given and fixed. Often, viral sequences are associated with various levels of uncertainty, not only in their associated metadata (e.g., sampling dates) but also with regard to sequencing quality. Typically, a quality control step removes unreliable sequences. In a Bayesian framework, one may integrate out sampling date uncertainty through their support so that sampling dates become parameters of the model and are no longer fixed (Pybus et al., 2012). The proposed algorithms and HMC machinery remain unaffected if one cycles between sampling all internal node heights and tip heights from their full conditional distributions. However, the derivative w.r.t. the height parameter in the ratio space needs to consider contributions from the tip nodes when one samples all node heights (including variable tip heights) jointly. Moreover, the anchor node and epoch constructions become variable and need to be jointly updated with tip heights. This remains an important avenue of future work.

5 Materials and Methods

We have implemented the algorithms in this manuscript within the development branch of the software package BEAST (Suchard et al., 2018) with likelihood computations off-loaded to the high-performance BEAGLE library (Ayres et al., 2019). We provide instructions and the BEAST XML files for reproducing these analyses on Github at https://github.com/suchard-group/hmc_divergence_time_manuscript_supplement.

6 Acknowledgments

The research leading to these results has received funding from the European Research Council under the European Union’s Horizon 2020 research and innovation programme (grant agreement no. 725422 - ReservoirDOCS). The Artic Network receives funding from the Wellcome Trust through project 206298/Z/17/Z. MAS and XJ are partially supported by NIH grants U19 AI135995, R56 AI149004, R01 AI153044 and R01 AI162611. GB acknowledges support from the Interne Fondsen KU Leuven / Internal Funds KU Leuven under grant agreement C14/18/094 and from the Research Foundation – Flanders (‘Fonds voor Wetenschappelijk Onderzoek – Vlaanderen’, G0E1420N and G098321N). PL acknowledges support by the Research Foundation – Flanders (‘Fonds voor Wetenschappelijk Onderzoek – Vlaanderen’, G066215N, G0D5117N and G0B9317N). JLT was supported by NSF DEB 1754142.

Bibliography

- Aiewsakun, P. and A. Katzourakis (2015). Time dependency of foamy virus evolutionary rate estimates. *BMC Evolutionary Biology* 15(1), 1–15.
- Andersen, K. G., B. J. Shapiro, C. B. Matranga, R. Sealfon, A. E. Lin, L. M. Moses, O. A. Folarin, A. Goba, I. Ochia, P. E. Ehiane, et al. (2015). Clinical sequencing uncovers origins and evolution of Lassa virus. *Cell* 162(4), 738–750.
- Andrieu, C., N. De Freitas, A. Doucet, and M. I. Jordan (2003). An introduction to MCMC for machine learning. *Machine Learning* 50(1-2), 5–43.
- Andrieu, C. and J. Thoms (2008). A tutorial on adaptive MCMC. *Statistics and Computing* 18(4), 343–373.
- Ayres, D. L., M. P. Cummings, G. Baele, A. E. Darling, P. O. Lewis, D. L. Swofford, J. P. Huelsenbeck, P. Lemey, A. Rambaut, and M. A. Suchard (2019). Beagle 3: improved performance, scaling, and usability for a high-performance computing library for statistical phylogenetics. *Systematic Biology* 68(6), 1052–1061.
- Baele, G., M. S. Gill, P. Lemey, and M. A. Suchard (2020). Hamiltonian Monte Carlo sampling to estimate past population dynamics using the skygrid coalescent model in a Bayesian phylogenetics framework. *Wellcome Open Research* 5(53), 53.
- Baele, G., P. Lemey, A. Rambaut, and M. A. Suchard (2017). Adaptive MCMC in Bayesian phylogenetics: an application to analyzing partitioned data in BEAST. *Bioinformatics* 33(12), 1798–1805.
- Biek, R., J. C. Henderson, L. A. Waller, C. E. Rupprecht, and L. A. Real (2007). A high-resolution genetic signature of demographic and spatial expansion in epizootic rabies virus. *Proceedings of the National Academy of Sciences* 104(19), 7993–7998.

- Bletsa, M., M. A. Suchard, X. Ji, S. Gryseels, B. Vrancken, G. Baele, M. Worobey, and P. Lemey (2019). Divergence dating using mixed effects clock modelling: An application to HIV-1. *Virus Evolution* 5(2), vez036.
- Casella, G. and R. L. Berger (2001). *Statistical Inference* (2nd ed.). Pacific Grove, CA: Duxbury.
- Dinh, V., A. Bilge, C. Zhang, and F. A. Matsen IV (2017). Probabilistic path hamiltonian monte carlo. In *Proceedings of the 34th International Conference on Machine Learning-Volume 70*, pp. 1009–1018. JMLR. org.
- Drummond, A. J., S. Y. Ho, M. J. Phillips, and A. Rambaut (2006). Relaxed phylogenetics and dating with confidence. *PLoS Biology* 4(5), e88.
- Düx, A., S. Lequime, L. V. Patrono, B. Vrancken, S. Boral, J. F. Gogarten, A. Hilbig, D. Horst, K. Merkel, B. Prepoint, et al. (2020). Measles virus and rinderpest virus divergence dated to the sixth century BCE. *Science* 368(6497), 1367–1370.
- Erwin, D. H., M. Laflamme, S. M. Tweedt, E. A. Sperling, D. Pisani, and K. J. Peterson (2011). The cambrian conundrum: early divergence and later ecological success in the early history of animals. *Science* 334(6059), 1091–1097.
- Fourment, M. and A. E. Darling (2019). Evaluating probabilistic programming and fast variational Bayesian inference in phylogenetics. *PeerJ* 7, e8272.
- Gill, M. S., P. Lemey, S. N. Bennett, R. Biek, and M. A. Suchard (2016). Understanding past population dynamics: Bayesian coalescent-based modeling with covariates. *Systematic Biology* 65(6), 1041–1056.
- Haario, H., E. Saksman, and J. Tamminen (1999). Adaptive proposal distribution for random walk Metropolis algorithm. *Computational Statistics* 14(3), 375–396.

- Hadfield, J., A. F. Brito, D. M. Swetnam, C. B. Vogels, R. E. Tokarz, K. G. Andersen, R. C. Smith, T. Bedford, and N. D. Grubaugh (2019). Twenty years of West Nile virus spread and evolution in the Americas visualized by Nextstrain. *PLoS Pathogens* 15(10), e1008042.
- Ho, S. Y., S. Duchêne, M. Molak, and B. Shapiro (2015). Time-dependent estimates of molecular evolutionary rates: evidence and causes. *Molecular Ecology* 24(24), 6007–6012.
- Ji, X., Z. Zhang, A. Holbrook, A. Nishimura, G. Baele, A. Rambaut, P. Lemey, and M. A. Suchard (2020). Gradients do grow on trees: a linear-time $O(N)$ -dimensional gradient for statistical phylogenetics. *Molecular Biology and Evolution* 37(10), 3047–3060.
- Kishino, H., J. L. Thorne, and W. J. Bruno (2001). Performance of a divergence time estimation method under a probabilistic model of rate evolution. *Molecular Biology and Evolution* 18(3), 352–361.
- Lartillot, N., M. J. Phillips, and F. Ronquist (2016). A mixed relaxed clock model. *Philosophical Transactions of the Royal Society B: Biological Sciences* 371(1699), 20150132.
- Lemey, P., S. L. Hong, V. Hill, G. Baele, C. Poletto, V. Colizza, Á. O’toole, J. T. McCrone, K. G. Andersen, M. Worobey, et al. (2020). Accommodating individual travel history and unsampled diversity in Bayesian phylogeographic inference of SARS-CoV-2. *Nature Communications* 11(1), 1–14.
- Lemey, P., A. Rambaut, J. J. Welch, and M. A. Suchard (2010). Phylogeography takes a relaxed random walk in continuous space and time. *Molecular Biology and Evolution* 27(8), 1877–1885.
- Mbala-Kingebeni, P., C. Pratt, M. Mutafali-Ruffin, M. G. Pauthner, F. Bile, A. Nkubandaye, A. Black, E. Kinganda-Lusamaki, M. Faye, A. Aziza, et al. (2021). Ebola Virus transmission Initiated by relapse of systemic Ebola virus disease. *New England Journal of Medicine* 384(13), 1240–1247.

- Membrebe, J. V., M. A. Suchard, A. Rambaut, G. Baele, and P. Lemey (2019). Bayesian inference of evolutionary histories under time-dependent substitution rates. *Molecular Biology and Evolution* 36(8), 1793–1803.
- Meredith, R. W., J. E. Janečka, J. Gatesy, O. A. Ryder, C. A. Fisher, E. C. Teeling, A. Goodbla, E. Eizirik, T. L. Simão, T. Stadler, et al. (2011). Impacts of the Cretaceous Terrestrial Revolution and KPg extinction on mammal diversification. *Science* 334(6055), 521–524.
- Metropolis, N., A. W. Rosenbluth, M. N. Rosenbluth, A. H. Teller, and E. Teller (1953). Equation of state calculations by fast computing machines. *The Journal of Chemical Physics* 21(6), 1087–1092.
- Neal, R. M. (2011). MCMC using Hamiltonian dynamics. *Handbook of Markov Chain Monte Carlo* 2(11).
- Pybus, O. G., M. A. Suchard, P. Lemey, F. J. Bernardin, A. Rambaut, F. W. Crawford, R. R. Gray, N. Arinaminpathy, S. L. Stramer, M. P. Busch, et al. (2012). Unifying the spatial epidemiology and molecular evolution of emerging epidemics. *Proceedings of the National Academy of Sciences* 109(37), 15066–15071.
- Rannala, B. and Z. Yang (2007). Inferring speciation times under an episodic molecular clock. *Systematic Biology* 56(3), 453–466.
- Roberts, G. O. and J. S. Rosenthal (2009). Examples of adaptive MCMC. *Journal of Computational and Graphical Statistics* 18(2), 349–367.
- Salvatier, J., T. V. Wiecki, and C. Fonnesbeck (2016). Probabilistic programming in Python using PyMC3. *PeerJ Computer Science*.
- Stan Development Team (2017). *Stan Modeling Language Users Guide and Reference Manual, Version 2.17.0*.

- Suchard, M. A., P. Lemey, G. Baele, D. L. Ayres, A. J. Drummond, and A. Rambaut (2018, Jan). Bayesian phylogenetic and phylodynamic data integration using beast 1.10. *Virus Evolution* 4(1), vey016.
- Thorne, J. L., H. Kishino, and I. S. Painter (1998). Estimating the rate of evolution of the rate of molecular evolution. *Molecular Biology and Evolution* 15(12), 1647–1657.
- Tierney, L. (1994). Markov chains for exploring posterior distributions. *the Annals of Statistics*, 1701–1728.
- World Health Organization (2021). Ebola outbreak 2018-2020- north kivu/ituri, drc <https://www.who.int/emergencies/situations/Ebola-2019-drc->.
- Zuckerkandl, E. and L. B. Pauling (1962). Molecular disease, evolution and genic heterogeneity. In M. Kasha and B. Pullman (Eds.), *Horizons in Biochemistry*, pp. 189–225. New York, NY: Academic Press.